JREE: Vol. 9, No. 4, (Autumn 2022) 85-100

Journal of Renewable Energy and Environment

Journal Homepage: www.jree.ir

Materials and Energy Research Center

MERC

Review Article

Maiden Application and Control Parameter Sensitivity Analysis of Fractional Order Tilt Integral Derivative Controller in Standalone Solar Photovoltaic System

Anupama Subhadarsini*, Babita Panda, Byamakesh Nayak

Department of Electrical Engineering Technology, School of Electrical Engineering, KIIT deemed to be University, Bhubaneswar, India.

PAPER INFO

Paper history:
Received: 31 October 2021
Revised in revised form: 12 February 2022
Scientific Accepted: 27 February 2022
Published: 08 October 2022

Keywords:
Fractional Order Controller,
Optimal Performance,
Error Minimization,
HGPSJO,
FOTIDC

ABSTRACT

The solar photovoltaic system is modeled in Simulink using Matlab. Boost converter, FOTIDC controller, and Reduced Switch Multilevel Inverter are all included in this PV system (RSMLI). With regard to solar photovoltaic systems, the focus of this study is on the Fractional Order Tilt Integral Derivative Controller (FOTIDC). In the suggested control technique, Hybrid Genetic Particle Swarm Jaya Optimization is used to optimize the control parameters (HGPSJO). Jaya Optimization (JO) is a hybrid of the Particle Swarm Optimization (PSO), Genetic Algorithm (GA), and GA/PSO algorithm optimization techniques, combining the best of each for improved control executions. Control performance is enhanced using a fractional calculus-based technique to redesign the Tilt Integral Derivative Controller (TIDC) in order to reduce noise and harmonic distortions. Harmonic distortion and voltage magnitude are reduced by applying the proposed control method to the PV system. Simulated Matlab environments are used to test the stability, robustness, and stability of the proposed system as well as its capacity to reduce harmonic distortions. It is also compared to other well-known control techniques in order to ensure that the real-time implementation is properly validated.

https://doi.org/10.30501/jree.2022.312874.1274

1. INTRODUCTION

Depleting reserves of conventional resources have forced researchers to focus on the renewable form of energy as an alternative [1]. Rapid developments in the field of solar energy have appeared recently. Over the years, numerous control methods such as Proportional Integral Derivative Controller (PIDC), fuzzy, adaptive, neuro, optimal, and fractional controllers have been studied [2-7].

The use of fractional order calculus in control theory has led to the advent of fractional order controllers. The basic reason for choice of fractional order controllers is because it is seen to demonstrate capabilities of suppressing chaotic behavior of mathematical models. A fractional-order calculus controller creates a distribution of time constant. This implies that there is no particular time constant or resonating frequency which, in turn, improves system responses. Fractional order controllers are seen to demonstrate the capabilities of suppressing chaotic behavior in mathematical models [8-12]. While being used as controllers, they serve various purposes. The basic purposes include the overall stability system enhancement [13, 14], robustness promotion [15], disturbance rejection ability against parameter uncertainties [16], voltage and current stabilization [17-20], enhanced dynamic response of the system [21], optimal dynamic performance [22], power flow control between source and load, ripple rejection [23], better performance under abnormal operating condition [24], computational burden reduction [25-30], flexibility of system [31], frequency stabilization, harmonic minimization [32], changing operating conditions [33], multi-criteria control of parameters, maintainance of average voltage across load under various operating conditions, hunting reduction, efficient transient tracking, regulation of output voltage, maintaining constant Direct Current (DC) link voltage, power factor control, and improved power quality [34]. Use of a prefilter in the controller enhances the controller response compared to traditional controller and it will give less overshoot to the system. PIDC suffers from large time delay and poor control for an integrating process forced to look for an alternative. TIDC is a great viable alternative. In TIDC, the proportional gain of PIDC is replaced by a tilted component. The tilted component is having a transfer function of s^n. The resultant transfer function of TIDCF represents an optimal transfer function which improves the feedback response of the controller [35, 36]. TIDC has better disturbance rejection ability, precise tuning, robustness, minimizes the impact of parameter deviations, better stabilization from internal and external disturbances, and enhances the feedback control as compared to PIDC. The control parameters (Tilt Gain (K_t), Integral Gain (K_i), Derivative Gain (K_d), Coefficient of tilt (n), angle of Integral (α), and angle of derivative (β) of FOTIDC

*Corresponding Author's Email: anupamasubhadarsini@gmail.com (A. Subhadarsini)
URL: https://www.jree.ir/article_158613.html

Please cite this article as: Subhadarsini, A., Panda, B. and Nayak, B., "Maiden application and control parameter sensitivity analysis of Fractional Order Tilt Integral Derivative Controller in standalone solar photovoltaic system", ***Journal of Renewable Energy and Environment (JREE)***, Vol. 9, No. 4, (2022), 85-100. (https://doi.org/10.30501/jree.2022.312874.1274).

are tuned for a better response. There are many tuning methods like Ziegler Nichols method of tuning, time domain tuning, and frequency domain tuning. The advent of optimization algorithms provides better tuning methods.

Genetic Algorithm (GA), Particle Swarm Optimization (PSO) and JO Algorithm are the optimization algorithms employed. The convergence rate of GA and PSO is low, while the convergence rate of JO is higher, since GA has the ability to get stuck at local minima and PSO has the ability to get trapped at global maxima. In order to overcome the primary shortcomings of GA, PSO, and JO, it is necessary to combine all three optimization algorithms to establish an approach that enjoys efficiency and robustness.

It is critical to boost the voltage generated by the solar panels after selecting and fine-tuning the controller. Because the voltage generated by solar panels is so low, it cannot be used directly; instead, a boost converter is used to boost it [37-40]. An inverter is used to transform this stepped-up voltage into Alternating Current (AC). By employing a Reduced Switch Multilevel Inverter (RSMLI), which uses the same number of sources as a cascaded h-bridge multilevel inverter, it employs less switches [41], which can be achieved. These switches are triggered by a performance-improving technology known as Third Harmonic Injected Sinusoidal Pulse Width Modulation (THISPWM). To achieve the intended objective, an attempt was made to devise a new strategy, which is formulated as follows:

- Designing a single-phase PV model in a MATLAB/SIMULINK environment.
- Designing a novel control strategy HGPSJO-tuned FOTIDC with THISPWM for the PV system in order to improve the system performance and reduce harmonic distortions.
- Employing harmonic distortion analysis of a suggested PV system to support its superior performance.
- Improvement of the proposed PV model's robustness.
- Performing comparative analysis to certify the superiority of the proposed approach.
- Conducting sensitivity analysis on FOTIDC parameters.

According to this plan, Section 2 gives mathematical models for boosting converters, THISPWM, and RSMLI. The filter design of the proposed model is also examined in this section. Section 3 provides a more in-depth explanation of FOTIDC. Section 4 focuses on results and performance analysis in great detail. Section 5 is a conclusion that takes the future potential into account.

2. FORMULATION OF THE PROBLEM

The major components of the FOTIDC-based photovoltaic system are photovoltaic cell, non-ideal boost converter, FOTIDC, THI-SPWM, and RSMLI. Figure 1(a-f) represents the basic circuit of photovoltaic cell, non-ideal boost converter, averaging model of boost converter, model of RSMLI, model of FOTIDC-based photovoltaic system, and block diagram of the overall proposed photovoltaic system. The inputs to the solar cell are irradiance and temperature. This generated voltage is DC in nature and is very low in magnitude; hence, it is fed to step-up converter to step up its magnitude. THISPWM-based triggering circuit provides the switching pulses to RSMLI. The PV system's detailed model is examined in the following sections.

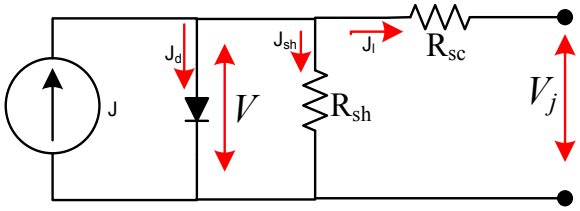

(a)

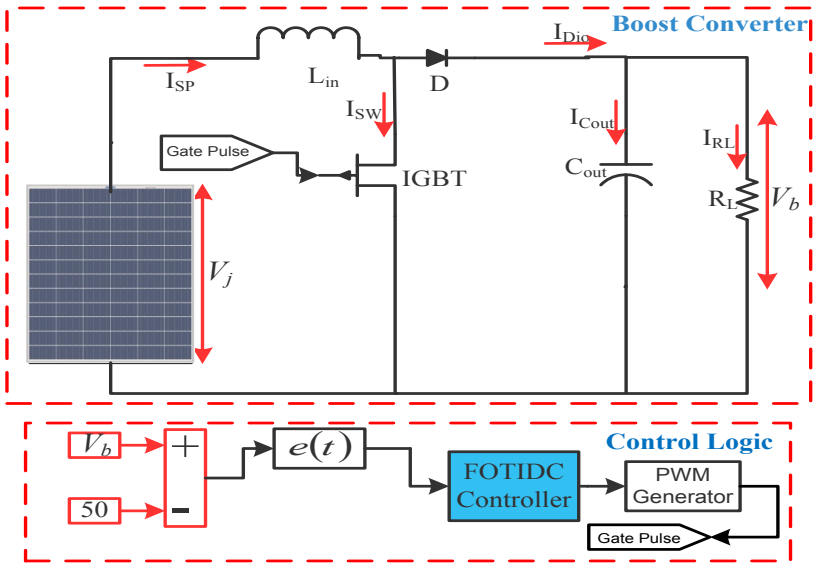

(b)

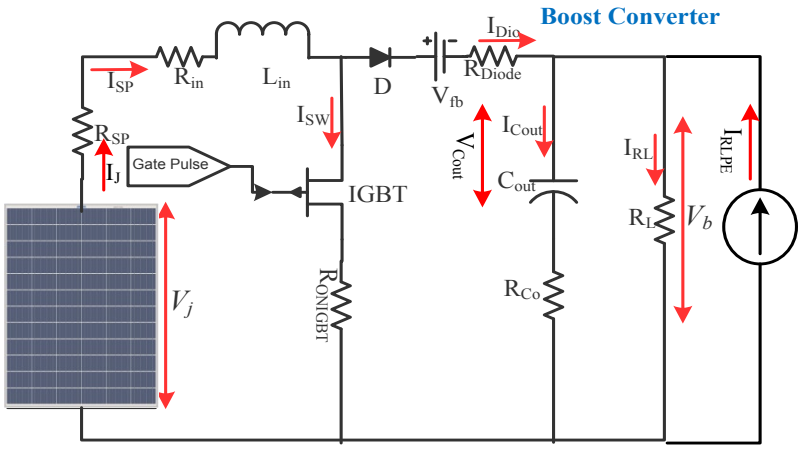
Boost Converter
I_{Dio}
I_{SP}
R_{in}
L_{in}
D
V_{fb}
R_{Diode}
I_{SW}
R_{SP}
I_J
Gate Pulse
IGBT
V_{Cout}
I_{Cout}
C_{out}
I_{RL}
I_{RLPE}
R_L
V_b
V_j
R_{ONIGBT}
R_{Co}

(c)

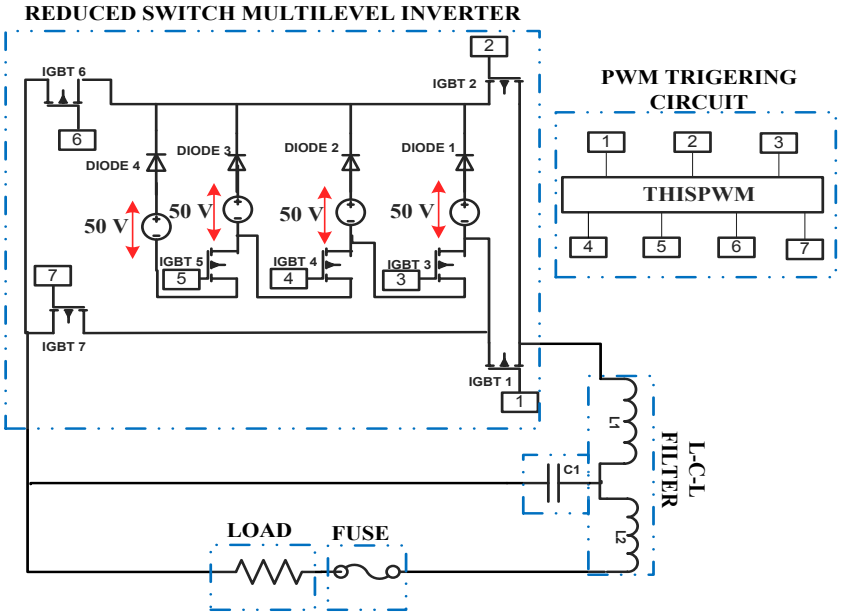
REDUCED SWITCH MULTILEVEL INVERTER
IGBT 6
IGBT 2
DIODE 4
DIODE 3
DIODE 2
DIODE 1
50 V
50 V
50 V
50 V
IGBT 5
IGBT 4
IGBT 3
IGBT 7
IGBT 1
PWM TRIGERING CIRCUIT
THISPWM
L1
C1
L2
L-C-L FILTER
LOAD
FUSE

(d)

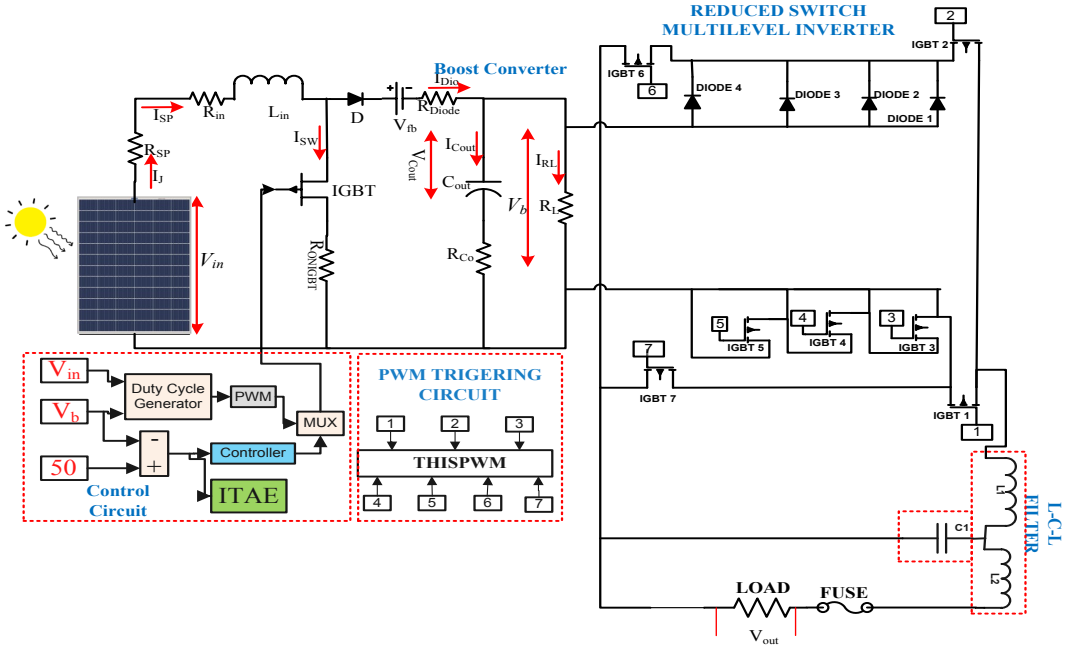
REDUCED SWITCH MULTILEVEL INVERTER
Boost Converter
I_{SP}
R_{in}
L_{in}
D
I_{Dio}
V_{fb}
R_{Diode}
I_{SW}
R_{SP}
I_J
IGBT
V_{Cout}
I_{Cout}
C_{out}
I_{RL}
V_b
R_L
R_{Co}
V_{in}
R_{ONIGBT}
IGBT 6
IGBT 2
DIODE 4
DIODE 3
DIODE 2
DIODE 1
IGBT 5
IGBT 4
IGBT 3
IGBT 7
IGBT 1
V_{in}
V_b
50
Duty Cycle Generator
PWM
MUX
Controller
ITAE
Control Circuit
PWM TRIGERING CIRCUIT
THISPWM
L1
C1
L2
L-C-L FILTER
LOAD
FUSE
V_{out}

(e)

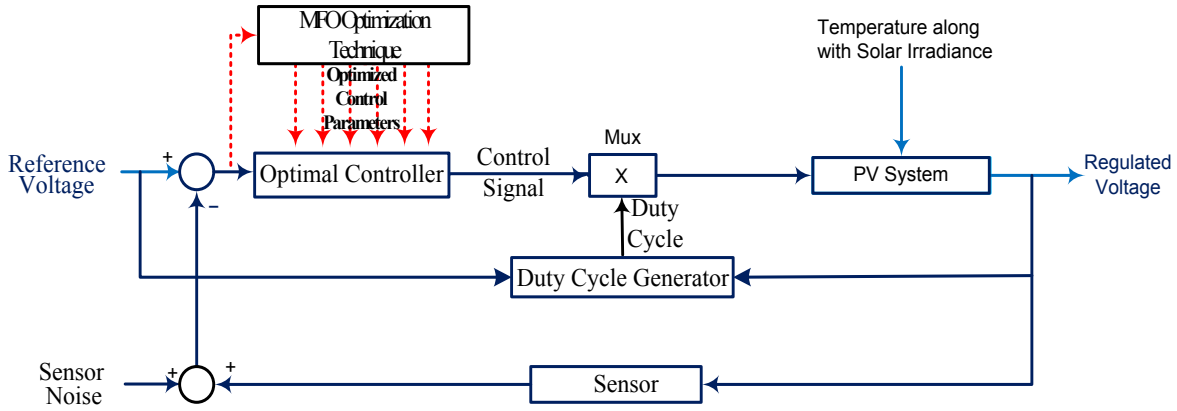

(f)

Figure 1. (a) Single diode model of solar PV cell, (b) Circuit diagram of boost converter, (c) Non-ideal model of boost converter, (d) Simulation model of the reduced switch multilevel inverter, (e) Model of FOTIDC-based photovoltaic system, and (f) Block Diagram of FOTIDC-based photovoltaic system

2.1. Photovoltaic cell

The photovoltaic cell is based on photo-electric effect which in turn depends on the presence of solar irradiance. Short-circuit current, open-circuit voltage, and maximum power point are the characteristics required for the design of photovoltaic cell. Figure 1(a) represents the equivalent circuit of the photovoltaic cell. Mathematically, the solar cell current can be represented as follows:

$$I = I_{pv} - I_O\left[\exp\left(\frac{qV}{akT}\right)\right] \tag{1}$$

Equation (1) fails to represent the characteristics of a photovoltaic array as there are several photovoltaic cells connected to form an array and it also requires additional parameters. This is achieved in Equation (2). The modified expression for the current generated by the photovoltaic cell is expressed as follows:

$$I = \frac{R_p}{R_s + R_p}\left(I_{PV} - I_0\left[\exp\left(\frac{V + R_s}{aV_t}\right) - 1\right] - \left(\frac{V}{R_p}\right)\right) \tag{2}$$

The summation of all structural resistances of the photovoltaic cell is represented by R_S. In order to compensate for the presence of leakage current in photovoltaic cell and different fabrication methods used by photovoltaic cell manufacturers, R_p is used. When the photovoltaic cell operates in the voltage source region, the influence of R_S is greater. Conversely, if the photovoltaic cell operates in the current source region, then the effect of R_p is greater. The value of R_S is lower than R_p. The standard value of R_S is taken in the range of 0.5-1.3 Ωcm^2. The standard value of R_p is taken in the range of 1-1000 $K\Omega cm^2$.

The energy generated by the photovoltaic cell is affected directly by the number of charge carriers present, which in turn depends upon the magnitude of solar irradiance incidences on the photovoltaic cell surface. I_{PV} in idyllic conditions is very difficult to determine as datasheets only inform about I_{SC}. Hence, it is assumed that for all photovoltaic cells, $I_{SC} \approx I_{PV}$. This assumption also holds ground as the value of R_S is lower than R_p. I_{PV} at (25 °C & 1 KW/m^2) depends upon solar irradiance and temperature and is mathematically expressed as:

$$I_{PV} = \left(\frac{R_S + R_P}{R_P} I_{SC} + K_I \Delta T\right)\frac{G}{G_n} \tag{3}$$

Mathematically, I_O can be represented as:

$$I_O = \frac{I_{SC} + K_I \Delta T}{\exp\left(\frac{V_{OC} + K_V \Delta T}{aV_t}\right) - 1}\left(\frac{T_n}{T}\right)^3 \exp\left[\frac{qE_g}{ak}\left(\frac{1}{T_n} - \frac{1}{T}\right)\right] \tag{4}$$

The diode identity factor is taken as 1.3. Upon substituting the values of I_{PV} and I_O into Equation (1), the modified expression for the current from photovoltaic cell is as follows:

$$I = \frac{R_p}{R_s + R_p}\left(\left(\frac{R_S + R_P}{R_P} I_{SC} + K_I \Delta T\right)\frac{G}{G_n} - \frac{I_{SC} + K_I \Delta T}{\exp\left(\frac{V_{OC} + K_V \Delta T}{aV_t}\right) - 1}\left(\frac{T_n}{T}\right)^3 \exp\left[\frac{qE_g}{ak}\left(\frac{1}{T_n} - \frac{1}{T}\right)\right]\left[\exp\left(\frac{V + R_s}{aV_t}\right) - 1\right] - \left(\frac{V}{R_p}\right)\right) \tag{5}$$

2.2. Boost converter

Boost converter steps up the magnitude of DC voltage. It is essential that the low voltages generated by solar arrays are in order of 20-25 volts and cannot be converted to alternating current quantities. Figure 1 (b) represents the model for boost converter. The boost converter consists of a diode (D), an Insulated Gate Bipolar Transistor (IGBT), a capacitor (C_{out}), and an inductor (L_{in}). In order to investigate the steady state and dynamical behaviour, it is essential to model the boost

converter dynamically. There are many methods to mathematically model the boost converter. Some of the populous methods include switching flow graph, averaging technique, state space technique, current injection technique, and bond graph method. All of these methods have their share of advantages and disadvantages. However, in most of these techniques, all elements of boost converter are considered ideal. Hence, an ideal control strategy is never formulated. When the elements are not considered ideal, then an effective and ideal switching technique is formulated. The boost converter is modeled by using a non-ideal state space averaging technique.

2.2.1. Non-ideal boost converter

The non-ideal model of boost converter is represented in Figure 1(c). The parasitic resistance and equivalent resistances are also represented in the circuit. R_{SP} represents the internal resistance of the PV system. R_{in} represents the Equivalent Series Resistance (ESR) of inductor. ESR value of the inductor is less than 1 Ω. The internal resistance of IGBT is represented by R_{ONIGBT}. The ESR resistance connected in series with C_{out} is R_{Co}. The typical value of R_{Co} is less than 1 Ω. The resistance of diode D is represented by R_{Diode}. The forward voltage drop of diode is represented by a voltage source, named as V_{fb}. The switching operation of IGBT present in boost converter is divided into two time frames. The time frames are on time and off time. The analysis is done separately for both on time and off time [3].

2.2.2. During IGBT on time

The input loop equation of the boost converter is represented by:

$$L_{in}\frac{dI_{SP}(t)}{dt} = -(R_{lin} + R_{ONIGBT} + R_{SP})I_{SP}(t) + V_j(t) \quad (6)$$

In order to analyse the non-ideal modelling of the boost converter, small perturbation is applied to the boost converter. This current perturbation is I_{RLPE}. The non-ideal model of the boost converter is represented in Figure 1(c, d). The current across capacitor C_{out} is represented in Equation (7).

$$I_{Cout}(t) = \frac{C_{out}dV_{Cout}(t)}{dt} = \frac{(R_L \| R_{Co})}{(R_L + R_{Co})}V_{Cout}(t) - \frac{(R_L \| R_{Co})}{R_{Co}}I_{RLPE}(t) \quad (7)$$

The output voltage is represented by Equation (8).

$$V_b(t) = \frac{(R_L \| R_{Co})}{(R_{Co})}V_{Cout}(t) - (R_L \| R_{Co})I_{RLPE}(t) \quad (8)$$

Equations (6-8) can be written in a state space equation form. The state variables are $Z_2(t) = |I_{SP}(t)\ V_{Cout}(t)|^T$, $u(t) = |V_b(t)\ I_{RLPE}(t)|^T$, and $y(t) = |V_b(t)\ I_J(t)|^T$.

$$\left.\begin{aligned} \dot{z}_2(t) &= A_{w1}z_2(t) + B_{w1}u(t) + G_{w1}V_{fb} \\ y(t) &= C_{w1}z_2(t) + E_{w1}u(t) + H_{w1}V_{fb} \end{aligned}\right\} \quad (9)$$

The state space matrices are represented below.

$$A_{w1} = \begin{vmatrix} \frac{-(R_{ONIGBT} + R_{in} + R_{SP})}{L_{in}} & 0 \\ 0 & -\frac{(R_L \| R_{Co})}{(C_{out}R_L R_{Co})} \end{vmatrix};$$

$$G_{w1} = |0 \quad 0|^T; \quad H_{w1} = |0 \quad 0|^T; \quad C_{w1} = \begin{vmatrix} 0 & \frac{(R_L \| R_{Co})}{(R_{Co})} \\ 1 & 0 \end{vmatrix};$$

$$B_{w1} = \begin{vmatrix} \frac{1}{L_{in}} & 0 \\ 0 & -\frac{(R_L \| R_{Co})}{(C_{out}R_{Co})} \end{vmatrix}; \quad E_{w1} = \begin{vmatrix} 0 & -(R_L \| R_{Co}) \\ 0 & 0 \end{vmatrix} \quad (10)$$

2.2.3. During IGBT off time

When IGBT is turned off and diode D is conducting, the input equation of boost converter is represented by:

$$L_{in}\frac{dI_{SP}(t)}{dt} = -\left((R_L + R_{Diode} + R_{SP}) + (R_L \| R_{Cout})\right)I_{SP}(t) - \frac{(R_L \| R_{Cout})}{R_{Cout}}V_{Cout}(t) + V_j(t) + (R_L \| R_{Cout})I_{RLPE}(t) - V_f \quad (11)$$

The current across capacitor C_{out} is represented in Equation (12).

$$I_{Cout}(t) = \frac{C_{out}dV_{Cout}(t)}{dt} = \frac{(R_L \| R_{Co})}{(R_{Co})}I_{RL}(t) - \frac{(R_L \| R_{Co})}{R_L R_{Co}}V_{Cout}(t) - \frac{(R_L \| R_{Co})}{(R_{Co})}I_{RLPE}(t) \quad (12)$$

The output voltage is represented by Equation (13).

$$V_b(t) = \frac{(R_L \| R_{Co})}{(R_{Co})}V_{Cout}(t) - (R_L \| R_{Co})I_{RLPE}(t) + (R_L \| R_{Co})I_{RL}(t) \quad (13)$$

Equations (11-13) can be written in the state space equation form. The state variables are $Z_2(t) = |I_{SP}(t)\ V_{Cout}(t)|^T$, $u(t) = |V_b(t)\ I_{RLPE}(t)|^T$, and $y(t) = |V_b(t)\ I_J(t)|^T$.

$$\left.\begin{aligned} \dot{z}_2(t) &= A_{w2}z_2(t) + B_{w2}u(t) + G_{w2}V_{fb} \\ y(t) &= C_{w2}z_2(t) + E_{w2}u(t) + H_{w2}V_{fb} \end{aligned}\right\} \quad (14)$$

The state space matrices are represented below.

$$A_{w2} = \begin{vmatrix} \frac{-(R_{Diode}+R_{SP}+R_L)+((R_L \| R_{Co}))}{L_{in}} & 0 \\ 0 & -\frac{(R_L \| R_{Co})}{(C_{out}R_L R_{Co})} \end{vmatrix};$$

$$B_{w2} = \begin{vmatrix} \frac{1}{L_{in}} & \frac{(R_L \| R_{Co})}{L_{in}} \\ 0 & -\frac{(R_L \| R_{Co})}{(C_{out}R_{Co})} \end{vmatrix}; \quad C_{w2} = \begin{vmatrix} (R_L \| R_{Co}) & \frac{(R_L \| R_{Co})}{(R_{Co})} \\ 1 & 0 \end{vmatrix};$$

$$E_{w2} = \begin{vmatrix} 0 & -(R_L \| R_{Co}) \\ 0 & 0 \end{vmatrix} \quad G_{w2} = \begin{vmatrix} \frac{-1}{L_{in}} & 0 \end{vmatrix}^T; \quad H_{w2} = \begin{vmatrix} 0 & 0 \end{vmatrix}^T; \quad (15)$$

The overall averaged non-ideal state space model of the boost converter is obtained by using Equations (9 and 14). The overall averaged non-ideal state space matrices are represented by Equation (16).

where D is duty cycle and $\tilde{D}$ = 1-D. The overall state space matrices of the averaged non-ideal model of the boost converter are represented by Equation (17).

$$\left.\begin{aligned} A_{avg} &= DA_{w1} + \tilde{D}A_{w2} \quad B_{avg} = DB_{w1} + \tilde{D}B_{w2} \quad C_{avg} = DC_{w1} + \tilde{D}C_{w2} \\ E_{avg} &= DE_{w1} + \tilde{D}E_{w2} \quad G_{avg} = DG_{w1} + \tilde{D}G_{w2} \quad H_{avg} = DH_{w1} + \tilde{D}H_{w2} \end{aligned}\right\} \quad (16)$$

$$A_{avg} = \begin{vmatrix} \frac{-\left(\left(DR_{ONIGBT} + \tilde{D}R_{Diode} + R_{SP} + R_{in}\right)\left(R_L + R_{Cout}\right) + D\tilde{D}R_L R C_{out}\right)}{L_{in}} & \frac{\tilde{D}\left(R_L \| R_{Co}\right)}{\left(L_{in}R_{Co}\right)} \\ \frac{\tilde{D}\left(R_L \| R_{Co}\right)}{\left(C_{out}R_{Co}\right)} & -\frac{\left(R_L \| R_{Co}\right)}{\left(C_{out}R_L R_{Co}\right)} \end{vmatrix}; \quad B_{avg} = \begin{vmatrix} \frac{1}{L_{in}} & \frac{\tilde{D}\left(R_L \| R_{Co}\right)}{L_{in}} \\ 0 & -\frac{\left(R_L \| R_{Co}\right)}{\left(C_{out}R_{Co}\right)} \end{vmatrix};$$

$$C_{avg} = \begin{vmatrix} \tilde{D}\left(R_L \| R_{Co}\right) & \frac{\left(R_L \| R_{Co}\right)}{\left(R_{Co}\right)} \\ 1 & 0 \end{vmatrix}; \quad E_{avg} = \begin{vmatrix} 1 & -\left(R_L \| R_{Co}\right) \\ 0 & 0 \end{vmatrix}; \quad G_{avg} = \begin{vmatrix} -\frac{\tilde{D}}{L_{in}} \\ 0 \end{vmatrix}; \quad H_{avg} = \begin{vmatrix} 0 \\ 0 \end{vmatrix} \quad (17)$$

The Transfer Function is defined as the ratio of Laplace transform of output to Laplace transform of input. The transfer function for the non-ideal boost converter is the ratio of output voltage to input voltage. This can be obtained by conducting small signal analysis of the non-ideal boost converter. Mathematically, it is expressed through Equation (18).

$$TF(s) = \frac{V_b(s)}{V_j(s)} = C_{avg}\left(sI - A_{avg}\right)^{-1}B_{avg} + E_{avg} \quad (18)$$

I is the unitary matrix and S is the Laplace operator.

2.3. Reduced switch multilevel inverter (RSMLI)

The stepped-up DC voltage from boost converter is fed to the inverter circuit to convert into AC. The choice of the inverter is the reduced switch multi-level inverter which is an improvised version of the cascaded h-bridge multilevel inverter. The improvisation made in cascaded h-bridge multilevel inverter technology is the reduction of effective switch count while keeping the number of sources the same [31-34]. The RSMLI is represented by Figure 1(d). The choice of RSMLI is listed out as follows:

- RSMLI manages to reduce voltage stress as compared to other inversion techniques.
- The use of transformers is naturally eliminated by choosing RSMLI.
- Total Harmonic Distortion (THD) values are lower.
- RSMLI has high-quality output with better electromagnetic compatibility.

Mathematically, the number of switches and sources required is dependent on the number of levels of RSMLI. The RSMLI used in this proposed manuscript is a 9-level RSMLI. Nine-level RSMLI is chosen because below 9-level harmonic distortion is dominant and above the 9-level mode, the triggering mechanism is becoming very complex, which tends to make the circuit redundant and often to reduce efficiency. Equations (19 and 20) give mathematical expressions for the quantity requirement of source and switches for the 9-level RSMLI.

$$\text{Number of sources} = \frac{\text{Level}-1}{2} \quad (19)$$

$$\text{Number of Controlled Switching devices} = \frac{\text{Level}+5}{2} \quad (20)$$

Level indicates the level of RSMLI. In this proposed manuscript from Equations (19 & 20) for 9-level RSMLI, the number of sources and controlled switches is 4 and 7, respectively. The switches include IGBT 1, IGBT 2, IGBT 3, IGBT 4, IGBT 5, IGBT 6, and IGBT 7. IGBT 1, IGBT 5,

IGBT 6, and IGBT 7 form the basis of bridge circuit of RSMLI. IGBT 1 and IGBT 5, IGBT 6, and IGBT 7 are connected as complimentary pairs. IGBT 1 and IGBT 5 are used to provide the negative half cycle, while the positive half cycle is provided by IGBT 6 and IGBT 7. IGBT 2, IGBT 3, and IGBT 4 are used when there is a need to supply the peak voltage. The reason for choosing 9-level RSMLI is:

- Below 9-level mode, harmonic disturbance is quite dominant making it difficult to operate;
- Above 9-level mode, the triggering mechanism becomes more complex;
- Soft switching technique is applicable to tuning of RSMLI; and
- In the case of higher level RSMLI, there is no sufficient reduction in harmonic.

2.3.1. Harmonics in RSMLI

Harmonic distortions present in electrical signals affect the power systems in many possible ways like heating effects, electromagnetic emissions, and an irritant trip of circuit breakers and reduction of power factors amongst many others [36]. A harmonic distortion present in electrical signals is measured by Total Harmonic Distortion (THD). THD is expressed mathematically through the expression Equation (21).

$$THD = \sqrt{\frac{((i_2)^2 + (i_3)^2 .....(i_n)^2)}{i_1}} \times 100\% \quad (21)$$

where the fundamental component is i_1, while i_2, i_3 … i_n represent the harmonic components. This situation calls for maintaining lower values of harmonics as lower value points to higher values of efficiency, power factor, and lower value of peak current.

2.4. Third harmonic injected sinusoidal pulse width modulation (THISPWM)

The triggering pulses for RSMLI are generated by PWM technique. The choice of PWM is taken as Third Harmonic Injected Sinusoidal Pulse Width Modulation (THI-SPWM) [35]. THI-SPWM as the name suggests that the third harmonic component is added to the sinusoidal reference. The addition of the third harmonic component to the sinusoidal reference improves the response of RSMLI. With reference to the sinusoidal signal, the harmonic injected is one-sixth of the amplitude. The peak magnitude of the carrier wave and modified sinusoidal reference are denoted by V_{car} and V_{ref}, respectively. The modified reference is represented mathematically by Equation (22).

$$V_{ref} = V_1 c_{max} \text{ Sin } (\omega t) + V_3 c_{max} \text{ Sin } (3\omega t) \quad (22)$$

where the fundamental component is represented by $V_1 c_{max}$ and injected third harmonic component is represented by $V_3 c_{max}$. The intersection of the carrier wave with the modified reference sets the operating point of THI-SPWM. The triggering pulse is generated after comparing the magnitudes of the carrier wave and the modified sinusoidal reference. If the magnitude of the modified wave is greater than that of carrier wave, then a positive trigger wave is generated, and vice versa. The extent to which modulation is done with a carrier signal is called as modulation index (m_a). Alternatively, m_a is defined as the relation between the ratios of modified reference voltages to carrier voltage. m_a is represented mathematically by Equation (23).

$$m_a = \frac{V_{ref}}{V_{car}} \quad (23)$$

The input voltage to RSMLI is V_b, while the Root Mean Square (RMS) value of the output of RSMLI is represented by V_{out} volts. The relationship between V_b and V_{out} is represented by Equation (24).

$$V_{out} = V_b \sqrt{\left(\sum_{b=1}^{2n} \frac{2T_{on}}{T \times \pi} \right)} \quad (24)$$

The time period is represented by T. The width of the n^{th} pulse is denoted by T_{on}.

2.5. Filter

The current and voltage signals from micro inverters often contain disturbances and harmonic components. The purpose of filter is to filter out unwarranted disturbances coming from micro inverter. A L-C-L type filter remains in the scope of this paper. The proposed filter has a better response than other types of filter. The base impedance (Z_b) for the proposed L-C-L type filter is expressed by Equation (25). Equation (26) and Equation (27) represent the mathematical formularies for base capacitance (C_b) and maximum values of load current (I_{max}), respectively.

$$z_b = V_{bn}{}^2 p_l^{-1} \quad (25)$$

$$C_b = (\omega_g Z_b)^{-1} \quad (26)$$

$$I_{max} = 0.333 * P\sqrt{2} * \left(V_f\right)^{-1} \quad (27)$$

The active power and the filter voltage are represented by P_l and V_f, respectively. A tolerance of 10 % is accommodated in the values of design parameters for robustness purposes. The change in load current accommodating 10 % variation and the value of inverter side inductance are given by Equations (28 and 29) separately. The switching frequency and DC link voltage are represented by f_{sw} and V_b, respectively.

$$\Delta I_{max} = 0.10 \times I_{max} \quad (28)$$

$$L_1 = \frac{V_b}{6 \times f_{sw} \times \Delta I_{max}} = \frac{V_b}{0.6 \times f_{sw} \times I_{max}} \quad (29)$$

A 10 % variation in the capacitance of the filter is allowed. Equation (30) represents the capacitance of the filter. The DC link side inductor is having a value of L_2 and is expressed mathematically by Equation (31).

$$C_f = 0.05 \times C_b \quad (30)$$

$$L_2 = \frac{\sqrt{\left(k_a^{-2}+1\right)}}{C_f \times \left(f_{sw}\right)^2} \quad (31)$$

The attenuation factor is represented by k_a. In order to compensate for the ripple effects, electromagnetic interference and resonance in a resistor with resistance (R_f) is inserted in series with a filter capacitor. The resonant frequency is denoted by f_{res}. The value of R_f is expressed mathematically by Equation (32).

$$R_f = (3C_f \times \omega_{res})^{-1} \quad (32)$$

Equations (25-32) help formulate a filter strategy for photovoltaic system, which is established in the simulation model, as shown in Figure 1(d, e).

2.6. Open loop analysis of photovoltaic system

The performance analysis of the open-loop model of the proposed PV system is analysed in the subsequent sub-sections.

2.6.1 Open-loop PV system's boost converter performance analysis

In the open-loop mode of the proposed PV system, the triggering pulse is provided through the pulse generator. IGBT is switched at 30 kHz. The voltage input is 20 volts. This value may increase up to 50 volts. The output voltage waveform for boost converter is represented in Figure 2. The output of the boost converter is fed as input to the inverter.

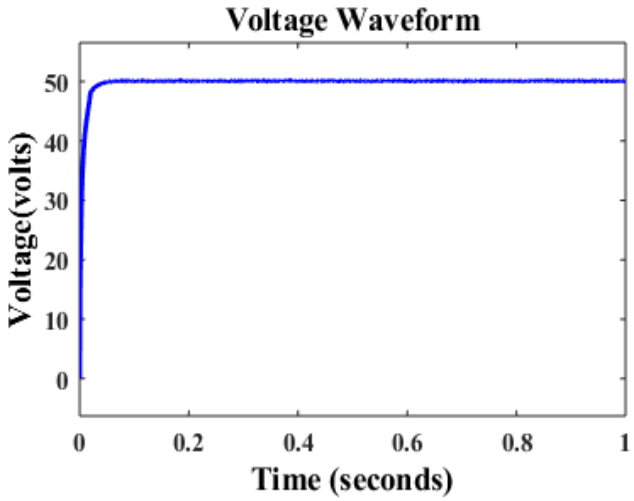

Figure 2. Boost converter response voltage waveform for the open-loop mode

2.6.2. Reduced switch multilevel inverter (RSMLI) performance analysis

The magnitude of the output voltage is 260 volts; this is represented in Figure 3(a). Figure 3(b) represents output current whose magnitude is 2.54 ampere. The load used is Resistive-Inductive (RL) load. The power is represented in Figure 3(c) having a magnitude of 670 watts. The waveform is not perfectly sinusoidal in nature and this loss in the waveform is due to nonlinearities present in the circuit. THD is a measure of the performance of the proposed circuit. The Voltage Total Harmonic Distortion (THD_V) was found to be 23.65 %, as depicted in Figure 4(a). However, Current Total Harmonic Distortion (THD_i) was found to be 23.07 %, as depicted in Figure 4(b).

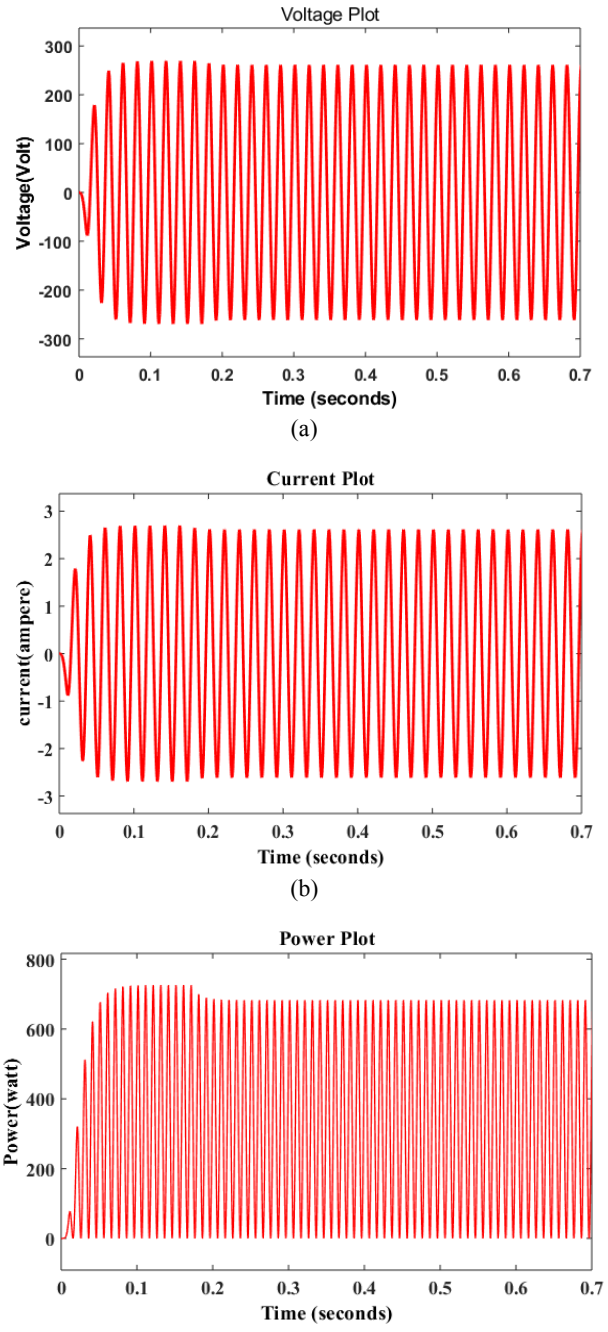

Figure 3. Responses of RSMLI of open-loop PV system: (a) Output voltage; (b) Output current; (c) Output power.

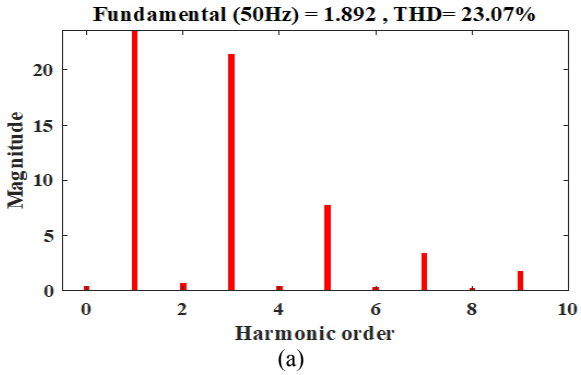

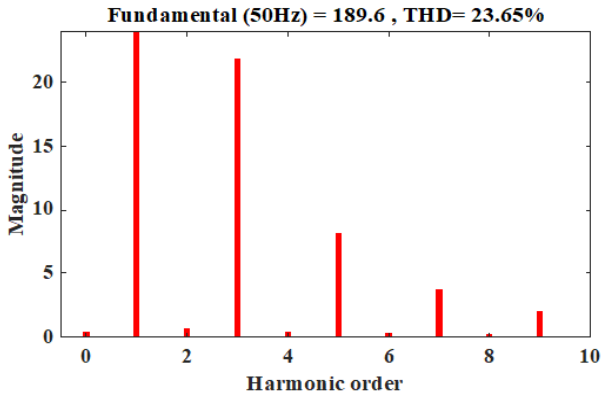

(b)

Figure 4. Performance plots for open-loop PV system: (a) Voltage harmonic analysis plot; (b) Current harmonic analysis plot.

According to Figures 3 and 4, the response of open-loop PV is not optimal and it requires an implementation of a controller. The FOTIDC is explained in the next section.

3. CONTROL ALGORITHM

The proposed control approach uses Tilt Integral Derivative Controller with Filter (TIDCF).

3.1. FOTIDC

FOTIDC is similar to PID controller. The major difference lies in the proportional gain of a compensator having a transfer function represented by $K_t s^{-n}$. For FOTIDC, the suitable value of n is taken between 2 and 3. It is chosen as 3 in this paper. This controller belongs to the family of fractional order controllers. The tilted behaviour provides a feedback gain as a function of frequency, which is tilted with respect to the gain of conventional compensator. The control signal ($U_{TID}(S)$) for the FOTIDC can be generated using the transfer function of the gain of the FOTIDC ($G_{TID}(S)$), error signal ($E_{TID}(S)$), reference signal ($R_{TID}(S)$), and output signal ($Y_{TID}(S)$). This is explained by Equations (33-35).

$$U_{TID}(S) = G_{TID}(S)E_{TID}(S) \tag{33}$$

$$E_{TID}(S) = R_{TID}(S) - Y_{TID}(S) \tag{34}$$

where

$$G_{TID(s)} = \frac{C_{OUT(s)}}{E_{TID(s)}} = K_t \times S^n + \frac{K_i}{S^\alpha} + K_d \times S^\beta \tag{35}$$

The control parameters (Tilt Gain(K_t), Integral Gain (K_i), Derivative Gain(K_d), Coefficient of tilt (n), angle of Integral (α), and angle of derivative (β)) of FOTIDC are tuned for better response. FOTIDC produces a higher degree of freedom in control parameters. FOTIDC is a Fractional Order controller. This serves good in eliminating disturbances quickly and efficiently. There is a need to optimize the control parameters of the controller. This is achieved through the application of a proper optimization algorithm.

3.2. Optimization algorithm

The advent of optimization algorithms provides better tuning methods. The optimization algorithms used are Genetic Algorithm (GA), Particle Swarm Optimization (PSO), and Jaya Algorithm (JA). These algorithms are hybridized and are applied to the parameter optimization of TIDCF. This is explained in sections appended below.

3.2.1. Genetic algorithm

Genetic Algorithm is a metaheuristically inspired process of natural selection that belongs to a larger class of evolutionary algorithms [3]. It obtains a high-quality solution to optimize and search problems using biological operators like mutation, crossover, and selection. A genetic algorithm requires a genetic representation of the solution and a fitness function to the solution domain.

3.2.2. Particle swarm optimization

PSO algorithm is one of the optimization techniques and a kind of evolutionary computation technique. It iteratively tries to improve or find a better solution with respect to a given measure of quantity [4]. PSO is a metahuristic as it makes no or the least number of assumptions about the problem being optimized and can search large spaces.

3.2.3. Jaya algorithm

Jaya algorithm always tries to get closer to success while avoiding failures. It tries to get closer to an optimal solution without being struck at any local minima and maxima [5]. The JA variables include population size, number of design variables, and termination criteria (iterations). The entire JAYA algorithm is based on Equation (23). The objective function is either to be minimized or maximized depending upon the proposed criteria for optimization. For any iteration i, it is assumed that m is the number of design variables and n is the number of candidates in a population. The best and worst solutions are represented by $X_{j,best,i}$ and $X_{j,worst,i}$ respectively. If $X_{j,k,i}$ is the value for the j^{th} variable, the k^{th} candidate of population during the i^{th} iteration is obtained. Then, the value is given by Equation (36).

$$X'_{l,n,i} = X_{l,n,i} + r_{1l,i}(X_{l,best,i} - |X_{l,n,i}|) - r_{2l,i}(X_{l,worst,i} - |X_{l,n,i}|) \tag{36}$$

where, $X'_{l,n,i}$ represents the new value of the controller parameter to be determined and $X_{l,n,i}$ represents the previously calculated value. $X_{l,best,i}$ and $X_{l,worst,i}$ represent the best and worst solutions of the optimization problem. $r_{1l,i}$ and $r_{2l,i}$ are two random variables for the l^{th} variable at the i^{th} iteration which have values between [0, 1], respectively.

3.2.4. Hybrid genetic particle swarm jaya algorithm (HGPSJA)

Hybrid Genetic Particle Swarm Jaya Algorithm (HGPSJA), as the name indicates, is a combination of 3 optimization algorithms. It combines the benefits of GA, PSO, and JA. This algorithm solves the problem of solution being struck at local minima or maxima. At first, PSO algorithm is employed to find the initial fit for the control parameters. Then, GA is applied to find intermediate fit of control parameter values. In the final step, JA is applied to find an optimal solution for the control parameters. The process is very swift and reduces the value of performance index to a very low value.

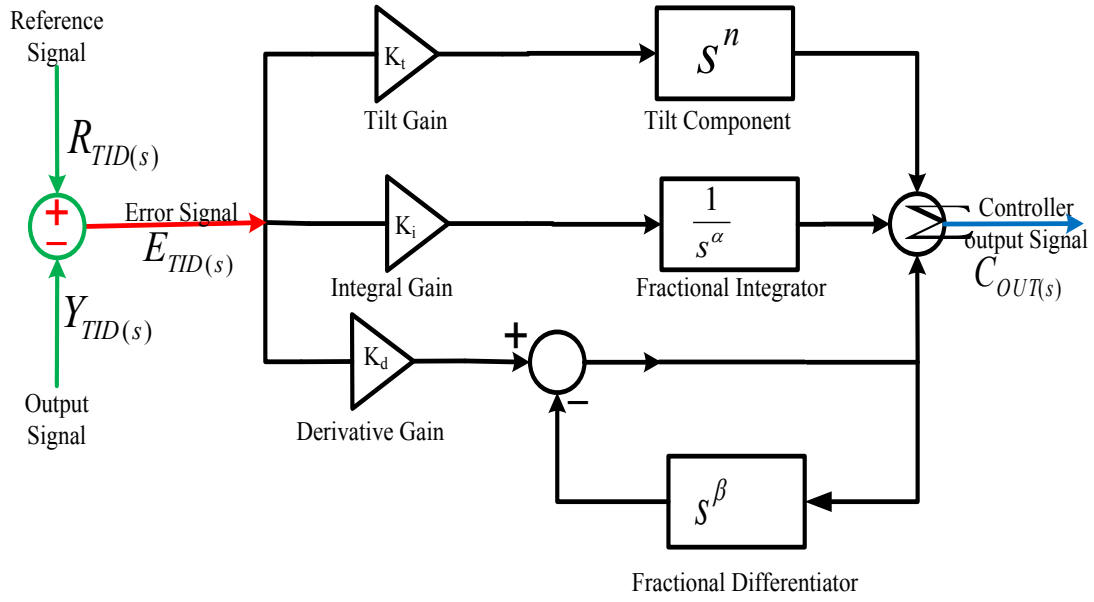

(a)

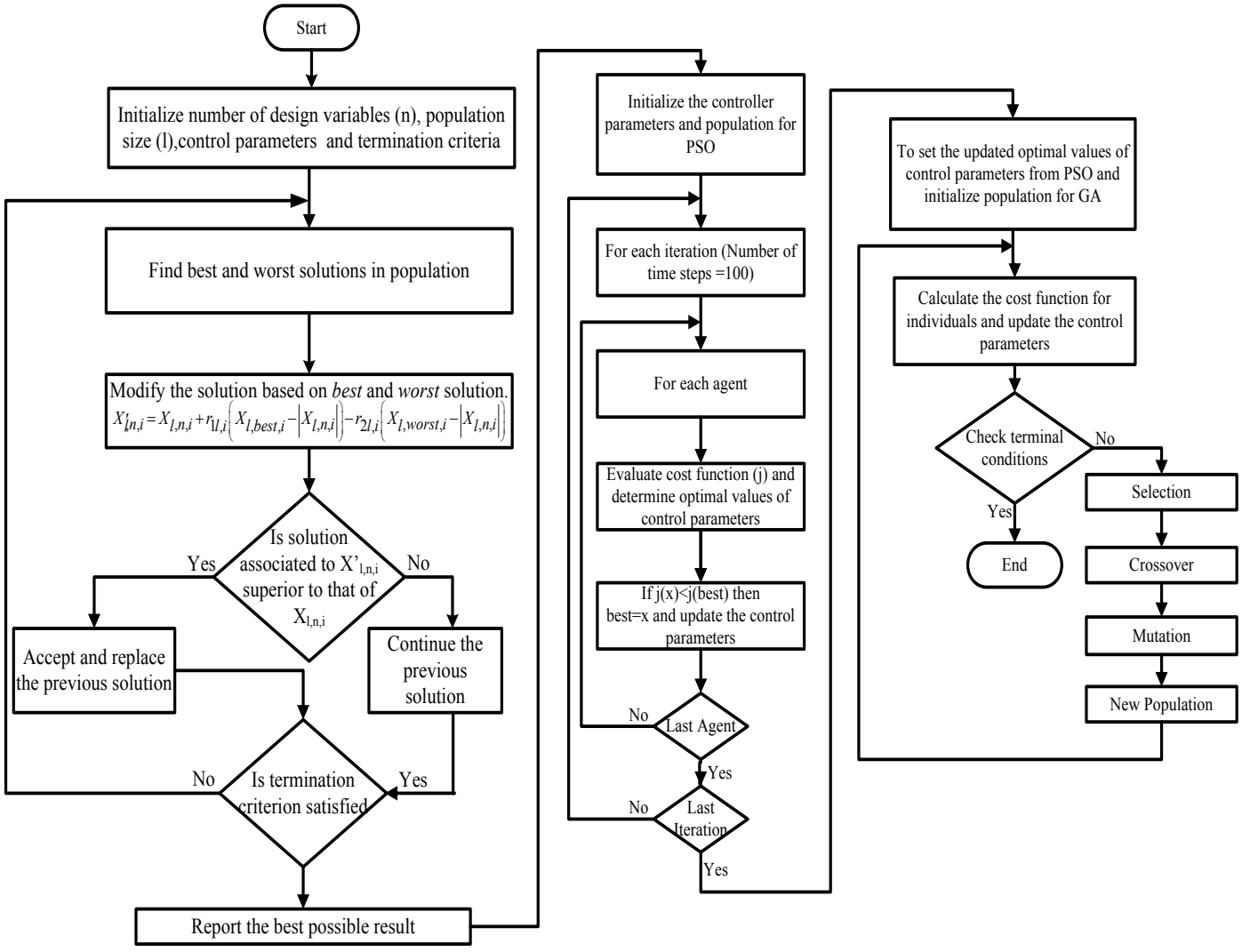

(b)

Figure 5. (a) Model of tilt integral derivative controller with filter (TIDCF), (b) Hybrid genetic particle swarm jaya algorithm (HGPSJA)

3.3. Cost function

A number of performance evaluation measures like maximum overshoot, peak time, settling time, rise time and damping ratio, etc. must be checked while designing a complex control system. However, it is not only a time consuming but also a hit-and-trial-based procedure. When input and operational conditions vary, it is cumbersome to analyse this measure. Performance index analysis has a selectivity feature which enables it to differentiate between optimal and non-optimal responses. Hence, the performance index criteria are good evaluation tools. Sensitivity of a controller can easily be predicted through analysis of its performance indexes. Performance index can be used as standard for controller design and optimization. Cost function and minimization or maximization function are closely related to each other. Hence, the cost function does play a role in designing and optimization of controllers. Broadly speaking, there are three performance indexes. They are Integral Time Absolute Error (ITAE), Integral Square Error (ISE), Integral Absolute Error (IAE). The mathematical equivalence is represented in Equation (37).

$$\left.\begin{aligned} \text{ITAE} &= \int t.\,|\,e(t)\,|\,dt \\ \text{IAE} &= \int |\,e(t)\,|\,dt \\ \text{ISE} &= \int |\,e(t)\,|^2\,dt \end{aligned}\right\} \quad (37)$$

ISE and IAE are less sensitive and computationally not compatible owing to these conditions; and ITAE is chosen as a performance index criterion. The parameters for different optimization algorithms are summarized in Table 1.

Table 1. Parameters of HGPSJO algorithm

Parameters	HGPSJO
No. of iterations	100
Mutation factor	0.7
Crossover factor	0.9
No. of population	200
No. of design variables	6
Cognitive factor	1.4
Social factor	1.4
Inertia weight	0.785
Random variable-1	1
Random variable-2	1

4. RESULT AND DISCUSSION

The detailed analysis of HGPSJA-tuned FOTIDC based closed-loop system is discussed in the appending sub-sections.

4.1. Closed loop response

The closed-loop or FOTIDC-based response of the proposed photovoltaic system is discussed in the sections appended below. The system is analysed in terms of performance, stability, and robustness.

4.1.1. Boost converter

The voltage generated by solar panels is so small that it is useless. As a result, the voltage must be increased in magnitude. A boost converter is employed to do this. In order to increase the voltage, it is escalated to 50 volts. Figure 6 depicts the situation.

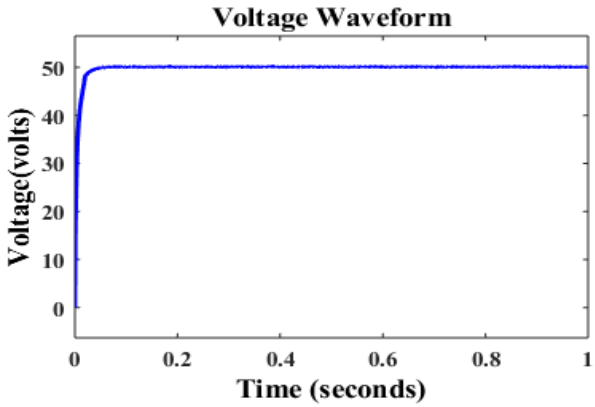

Figure 6. DC voltage output of the boost converter

4.1.2. RSMLI

RSMLI receives this boosted voltage. This, then, converts the voltage to an alternating one. This induced voltage has a magnitude of 254 volts. It is represented in Figure 7. The inverter is connected to a load of $100 + 240e^{-3}$ j Ω. The steady-state current generated by the load is 2 amperes, as given in Figure 8. As shown in Figure 9, the load draws 508 watts of electricity.

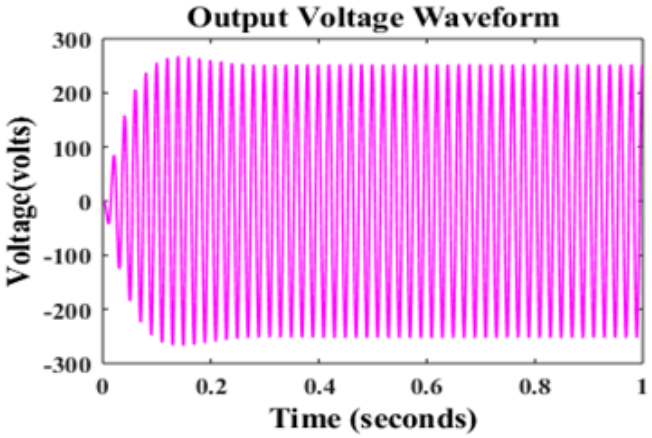

Figure 7. Output voltage of RSMLI

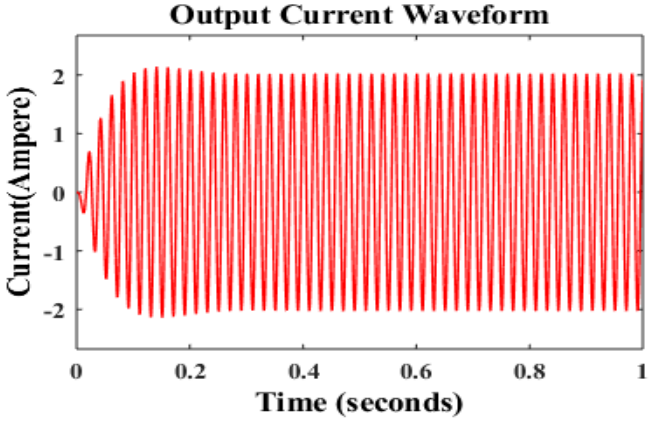

Figure 8. Output current of RSMLI

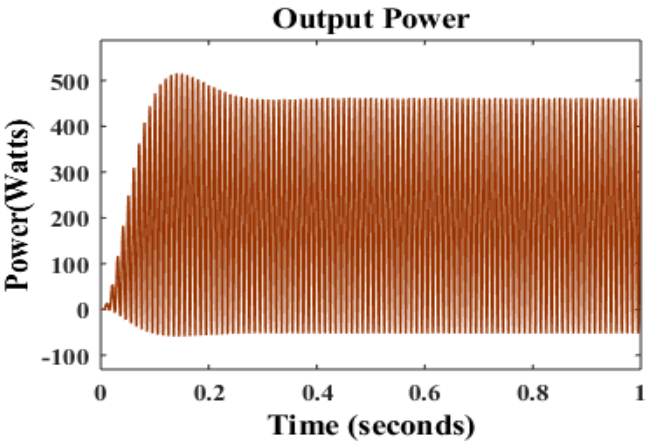

Figure 9. Output power of RSMLI

4.1.3. Robustness

Figure 10 (a-d) represents the variation in temperature, irradiance, fluctuation of boost converter output voltage, and fluctuation of RSMLI (inverter) output voltage. Boost converter output voltage fluctuates from 49 volts at 800 watt/m^2 to 53 at 1150 watt/m^2. Inverter voltage fluctuates from 249 volts to 256 volts. Solar power generation can be fluctuatory in nature. Hence, a power system frequency response plot indicates the efficacy and effectiveness of the proposed model.

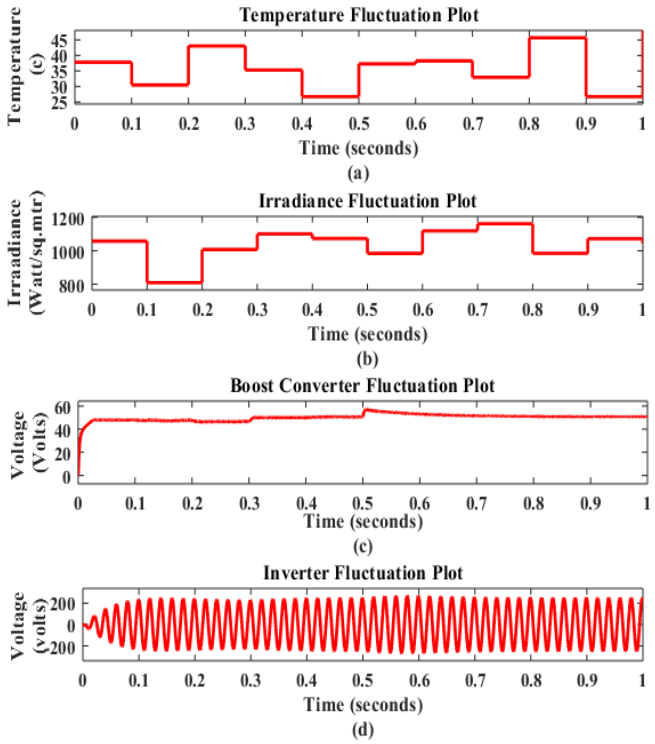

Figure 10. (a) Variation of temperature with time; (b) Variation of irradiance with time; (c) fluctuation of boost converter output voltage with change in irradiance and temperature; (d) fluctuation of RSMLI (inverter) output voltage with fluctuation in irradiance and temperature

4.1.4. Stability

Stability of any controller or for the matter of the entire proposed PV system is essential to any validation of the model. The proposed model is analysed for a wide range of frequency spectra. The proposed model is analysed for stability based on Matignon stability theorem. Dynamic system stability analysis of linear time invariant system suggests that the all roots of the characteristic equation should lie on the left and side of s-plane and should be away from origin [44]. However, it is not the case in fractional order controllers. The stability of fractional order system is based on Matignon stability theorem, stating that a fractional order system G(s) is stable if it satisfies Equation (38). In this equation, σ is seen as a symbol for the Laplace variable s. i represents the ith root of characteristic equation and q is the order of integral. Figure 11 represents the stability curve for fractional-order (FOTIDC) closed-loop system.

$$\left|\arg\left(\sigma_i\right)\right| = q\frac{\pi}{2}, \left\{\sigma = s^q : q \ni \left(0 \le q \le 2\right) : \forall \sigma_i \in C\right\} \quad (38)$$

As shown in Figure 11, the suggested model is able to handle higher-order frequency responses with ease.

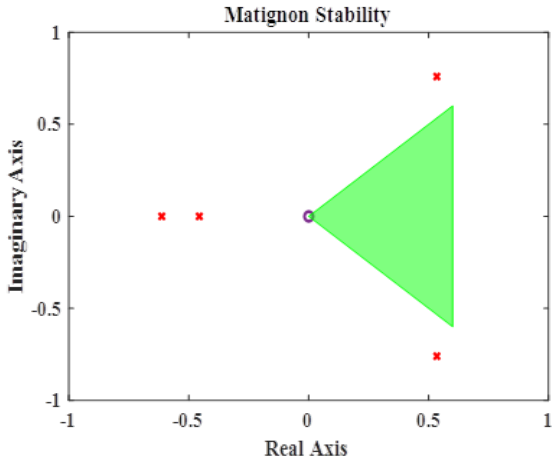

Figure 11. Stability (Matignon stability plot) of the proposed system

4.2. Harmonic analysis

Components of frequency other than fundamental component form the harmonic. This harmonic causes the irrational behaviour of the proposed system. The harmonic induced in system is current harmonic (THD$_i$) and it induces harmonic disturbance in voltage component, which is known as voltage harmonic (THD$_v$). THD$_i$ and THD$_v$ for the proposed system are represented in Figure 12 (a, b), respectively.

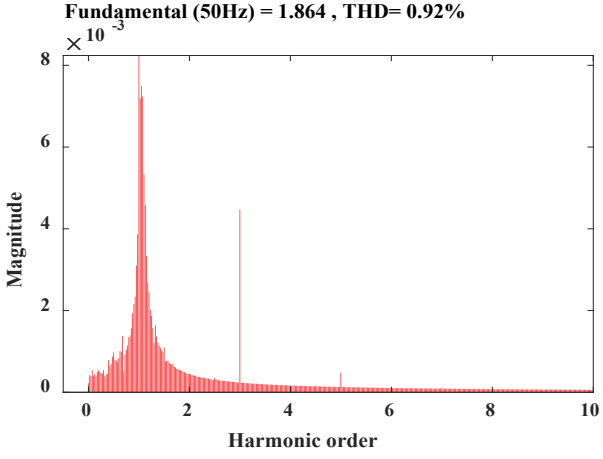

(a)

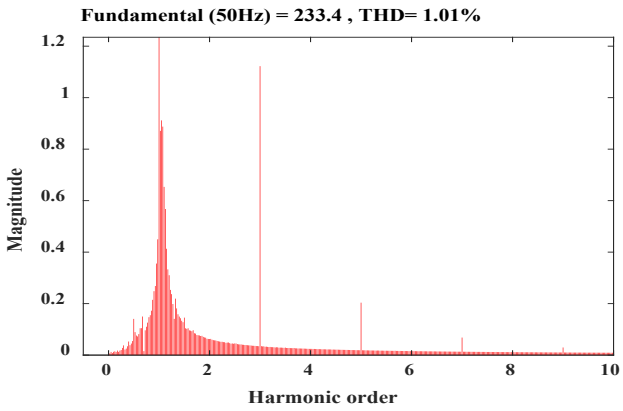

(b)

Figure 12. Total harmonic distortion curve for RSMLI: (a) THD_i and (b) THD_v plots

4.3. Frequency control

The proposed model also provides frequency control apart from making the system robust and stable. Figure 13 (a, b) represents frequency and angular frequency plot along time. Less fluctuations in frequency appear with a peak of 50.23 Hz. This, in turn, indicates that the proposed model maintains good power quality even when the system in itself is projected to fault.

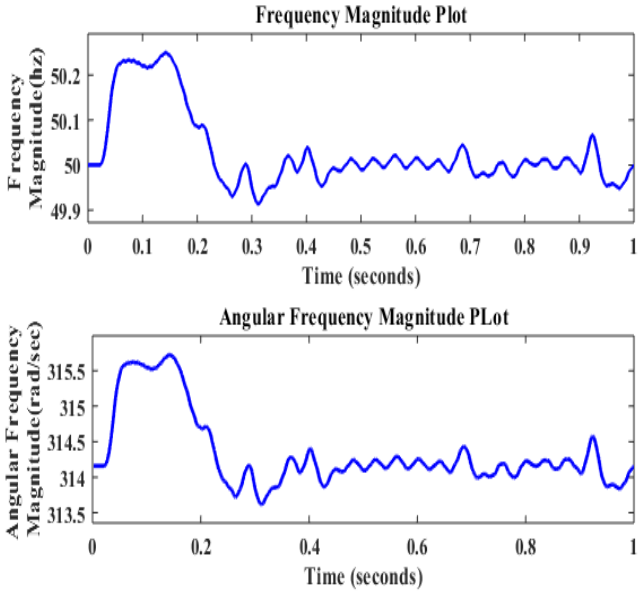

Figure 13. (a) Magnitude of frequency variation with respect to time; (b) Magnitude of angular frequency variation with respect to time

5. SENSITIVITY ANALYSIS

The model is a mathematical approximation of actual system. The controllers designed for the nominal model often provide suitable performance as per nominal model requirements. However, they may not satisfy the control objective of the actual system. Sensitivity analysis is performed on the performance of the controller in the presence of model uncertainties. The use of sensitivity analysis is to evaluate how the parameters of the proposed model influence the model output or model design requirements. Sensitivity analysis is defined as the study of how uncertainty in the output of a model can be attributed to different sources of uncertainty in the model input. Mathematically, the sensitivity of the cost function with respect to certain parameters is equal to the partial derivative of the cost function with respect to those parameters. There are two types of sensitivity analysis. They are local sensitivity analysis and global sensitivity analysis. Local sensitivity analysis is a One-At-a-Time (OAT) technique. OAT techniques analyse the effect of one parameter on the cost function at a time, thus keeping the other parameters fixed.

They explore only a small fraction of the design space, especially when there are many parameters. Also, they do not provide an insight into how the interactions between parameters influence the cost function. Global sensitivity analysis is often implemented using Monte Carlo techniques. This approach uses a representative (global) set of samples to explore the design space. The objective of the sensitivity analysis for the proposed model is to reduce THD and maximize output voltage while reducing cost function (ITAE). The control parameter variation plot is represented in Figure 14(a), and Figure 14(b) represents the THD variation plot. It is evident that in order to minimize THD, the optimized values of control parameters are not prone to sensitivity fluctuations. This is evident from 0.0008 variations in THD value.

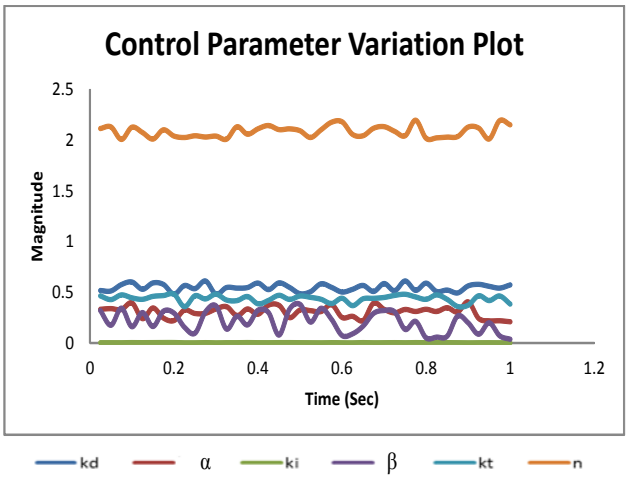

(a)

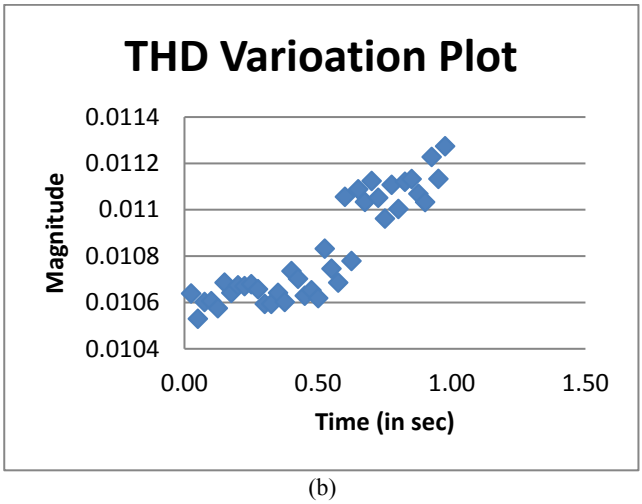

(b)

Figure 14. (a) FOTIDC control parameter variation plot; (b) THD variation with fluctuation of control parameter

5.1. Comparative study

The performance of the proposed system is compared with those of other controllers and from Table 2, it is evident that

the proposed system has outperformed all state-of-the-art controllers. The proposed system is compared with others in terms of harmonic, system stability, robustness, and frequency control.

Table 2. Comparative analysis

Parameter	Fractional proportional-resonant current controllers [19]	Adaptive PI controller [28]	Adaptive PI controller [17]	Fuzzy logic based PV system [5]	PR controller based PV system [15]	Proposed model
THD_i in %	7.2	5.06	4.27	3.37	1.19	1.02
THD_v in %	3.2	2.86	-	-	-	0.91
Stability	Less	Less	Less	Less	Less	More
Robust	Less	Less	Less	Less	Less	More
Frequency control	No	No	No	No	No	Yes

6. CONCLUSIONS

In the proposed PV system, the total harmonic distortion was reduced due to the application of HGPSJO-tuned FOTIDC in a PV system, thus resulting in improvements in its accuracy, stability, and robustness. The proposed model was tested against sudden changes in solar irradiance. The performance was as expected. The proposed work was seen to reduce harmonic distortion. The use of THISPWM in the implementation of HGAPSO-tuned FOTIDC-based PV system enhanced its overall performance by facilitating the suppression of harmonic distortions and there by improvement of stability and robustness. The concomitant enhanced performance of the proposed HGPSJO-tuned FOTIDC-based PV system enjoyed better accuracy, more robustness, and higher stability through the capability to bear irradiance fluctuations as validated in real time.

7. ACKNOWLEDGEMENT

The authors would like to thank Prof. Chinmaya Kumar Panigrahi for his comments and insightful suggestions about the manuscript. This research was supported by the School of Electrical Science, Kalinga Institute of Industrial Technology, Bhubaneswar, India.

NOMENCLATURE

I	Solar cell current (Ampere)
I_{PV}	Photo current (Ampere)
I_0	Cell reverse saturation current (Ampere)
a	Diode identity factor
q	Charge of electron (coloumb)
K	Boltzmann constant (joule per kelvin)
ΔT	Change in temperature (K)
G_n	Solar nominal irradiation (KW/m^2)
G	Solar actual irradiation (KW/m^2)
V_{OC}	Nominal open circuit voltage (volt)
T	Temperature (K)
V_t	Terminal voltage $V_t = \frac{kT}{q}$ (volt)
R_p	Shunt resistance (Ω)
R_s	Series resistance (Ω)
I_{SC}	Short- circuit current (Ampere)
K_I	Short- circuit temperature (Ampere)
K_v	Voltage/temperature coefficient (ppm/°C)
N_s	Series-connected cells
T_n	Nominal temperature (K)
J_O	Current density of the semiconductor (ampere/m^2)

Subscript

PV	Photovoltaic Cell
n	Nominal
SC	Short circuit
p	Shunt
I	Short circuit temperature
OC	Open circuit
O	Output
t	Terminal voltage
s	Series
V	Voltage coefficient

REFERENCES

1. Shakouri, M., Ghadamian, H. and Noorpoor, A., "Quasi-dynamic energy performance analysis of building integrated photovoltaic thermal double skin façade for middle eastern climate case", ***Applied Thermal Engineering***, Vol. 179, (2020), 115724. (https://doi.org/10.1016/j.applthermaleng.2020.115724).
2. Gopal, Y., Birla, D. and Lalwani, M., "Reduced switches multilevel inverter integration with boost converters in photovoltaic system", ***SN Applied Sciences***, Vol. 2, No. 1, (2020), 1-15. (https://doi.org/10.1007/s42452-01).
3. Janardhan, K., Mittal, A. and Ojha, A., "A symmetrical multilevel inverter topology with minimal switch count and total harmonic distortion", ***Journal of Circuits, Systems and Computers***, Vol. 29, No. 11, (2020). (https://doi.org/10.1142/S0218126620501741).
4. Mukundan, C.N., Jayaprakash, P., Subramaniam, U. and Almakhles, D.J., "Binary hybrid multilevel inverter-based grid integrated solar energy conversion system with damped SOGI control", ***IEEE Access***, Vol. 8, (2020), 37214-37228. (https://doi.org/10.1109/ACCESS.2020.2974773).
5. Gopal, Y., Birla, D. and Lalwani, M., "Selected harmonic elimination for cascaded multilevel inverter based on photovoltaic with fuzzy logic control maximum power point tracking technique", ***Technologies,*** Vol. 6, No. 3, (2018), 62-79.(https://doi.org/10.3390/technologies6030062).
6. Babkrani, Y., Naddami, A. and Hilal, M., "A smart cascaded H-bridge multilevel inverter with an optimized modulation techniques increasing the quality and reducing harmonics", ***International Journal of Power Electronics and Drive Systems***, Vol. 10, No. 4, (2019), 1852-1862. (https://doi.org/10.11591/ijpeds.v10.i4.1852-1862).
7. Mhiesan, H., Wei, Y., Siwakoti, Y.P. and Mantooth, H.A., "A fault-tolerant hybrid cascaded H-bridge multilevel inverter", ***IEEE Transactions on Power Electronics***, Vol. 35, No. 12, (2020), 12702-12715. (https://doi.org/10.1109/TPEL.2020.2996097).
8. Doostinia, M, Beheshti, M.T.H., Alavi, S.A. and Guerrero J.M., "Distributed control strategy for DC microgrids based on average consensus and fractional-order local controllers", ***IET Smart Grid***, Vol. 4, No. 8, (2021),1-12. (https://doi.org/10.1049/stg2.12038).
9. Guha, D.R., Banerjee, P.K., Padmanaban, S., Blaabjerg, S. and Chittathuru, D., "Small-signal stability analysis of hybrid power system with quasi-oppositional sine cosine algorithm optimized fractional order PID controller", ***IEEE Access***, Vol. 8, (2020), 155971-155986. (https://doi.org/10.1109/ACCESS.2020.3018620).
10. Djebbri, S., Ladaci, S., Metatla, A. and Balaska, H., "Fractional-order model reference adaptive control of a multi-source renewable energy

system with coupled DC/DC converters power compensation", ***Energy Systems***, Vol. 11, No. 2, (2020), 315-355. (https://doi.org/10.1007/s12667-018-0317-5).

11. Shakouri, M., Noorpoor, A. and Ghadamian, H., "Quantification of thermal energy performance improvement for building integrated photovoltaic double-skin façade using analytical method", ***Journal of Renewable Energy and Environment (JREE)***, Vol. 7, No. 3, (2020), 56-66. (https://dx.doi.org/10.30501/jree.2020.228559.1105).
12. Shakoori, M., Noorpoor, A., Golzari, S. and Zamen, M., "Energy simulation and parametric analysis of water cooled photovoltaic/thermal system", ***Amirkabir Journal of Mechanical Engineering***, Vol. 50, No. 6, (2019), 1361-1374. (https://dx.doi.org/10.22060/mej.2017.12703.5402).
13. Ramadan, H.S., "Optimal fractional order PI control applicability for enhanced dynamic behavior of on-grid solar PV systems", ***International Journal of Hydrogen Energy***, Vol. 42, No. 7, (2017), 4017-4031. (https://doi.org/10.1016/j.ijhydene.2017.01.122).
14. Shakouri, M., Ebadi, H. and Gorjian, S., "Solar photovoltaic thermal (PVT) module technologies", In ***Photovoltaic Solar Energy Conversion***, Academic Press, Vol. 1, No. 1, (2020), 79-116. (https://doi.org/10.1016/B978-0-12-819610-6.00004-1).
15. Fallah Ardashir, J., Mohammadpour, S.A., Khoun-Jahan, H. and Sabahi, M.,"Fractional PR control of a grid tied flying capacitor inverter for PV applications", ***Journal of Energy Management and Technology***, Vol. 3, No. 2, (2019), 58-64. (https://dx.doi.org/10.22109/jemt.2019.143673.1116).
16. Yousef, A.M., Abo-Elyousr, F.., Elnozohy, A., Mohamed, M. and Abdelwahab, S.A.M., "Fractional order PI control in hybrid renewable power generation system to three phase grid connection", ***International Journal on Electrical Engineering and Informatics***, Vol. 12, No. 3, (2020), 470-493. (https://dx.doi.org/10.15676/ijeei.2020.12.3.5).
17. Merai, M., Naouar, M.W., Slama-Belkhodja, I. and Monmasson, E., "An adaptive PI controller design for DC-link voltage control of single-phase grid-connected converters", ***IEEE Transactions on Industrial Electronics***, Vol. 66, No. 8, (2018), 6241-6249. (https://doi.org/10.1109/TIE.2018.2871796).
18. Swarnakar, J., Sarkar, P. and Singh, L.J., "Direct discretization method for realizing a class of fractional order system in delta domain–a unified approach", ***Automatic Control and Computer Sciences***, Vol. 53, No 2, (2019), 127-139. (https://doi.org/10.3103/S014641161902007X).
19. Heredero-Peris, D., Chillón-Antón, C., Sánchez-Sánchez, E. and Montesinos-Miracle, D., "Fractional proportional-resonant current controllers for voltage source converter", ***Electric Power Systems Research***, Vol. 168, (2019), 20-45. (https://doi.org/10.1016/j.epsr.2018.09.014).
20. Zhang, S., Wei, J., Xu, Z., Tang, B. and Niu, R., "Research on the influence of system parameters on the electromechanical dynamics of a large wind turbine drivetrain", ***Energy Reports***, Vol. 7, (2021), 7835-7851. (https://doi.org/10.1016/j.egyr.2021.11.020).
21. Ahmed, T., Waqar, A., Elavarasan, R.M., Imtiaz, J., Premkumar, M. and Subramaniam, U., "Analysis of fractional order sliding mode control in a D-STATCOM integrated power distribution system", ***IEEE Access***, Vol. 9, (2021), 70337-70352. (https://doi.org/10.1109/ACCESS.2021.3078608).
22. Nicola, M. and Nicola, C.I., "Fractional-order control of grid-connected photovoltaic system based on synergetic and sliding mode controllers", ***Energies***, Vol. 14, No. 2, (2021), 510-535. (https://doi.org/10.3390/en14020510).
23. Darvish, F.A., "Optimal fractional order BELBIC to ameliorate small signal stability of interconnected hybrid power system", ***Environmental Progress and Sustainable Energy***, Vol. 38, No. 5, (2019), 13208, 1-23. (https://doi.org/10.1016/j.est.2021.102983).
24. Kakkar, S., Maity, T., Ahuja, R.K., Walde, P., Saket, R.K., Khan, B. and Padmanaban, S., "Design and control of grid-connected PWM rectifiers by optimizing fractional order PI controller using water cycle algorithm", ***IEEE Access***, Vol. 9, (2021), 125941-125954. (https://doi.org/10.1109/ACCESS.2021.3110431).
25. Zamee, M.A. and Dongjun W., "A novel plant propagation-based cascaded fractional order PI controller for optimal operation of grid-connected single-stage three-phase solar photovoltaic system", ***Applied Sciences***, Vol. 9, No, 20, (2019), 4269-4290. (https://doi.org/10.3390/app9204269).
26. Ozan, G.Ü.L. and Nusret, T.A.N., "Voltage control at building integrated photovoltaic and wind turbine system with PI-PD controller", ***Avrupa Bilim ve Teknoloji Dergisi***, Vol. 18, (2020), 992-1003. (https://doi.org/10.31590/ejosat.668427).
27. Guel-Cortez, A.J., Méndez-Barrios, C.F., González-Galván, E.J., Mejía-Rodríguez, G. and Félix, L., "Geometrical design of fractional PDμ controllers for linear time-invariant fractional-order systems with time delay", ***Proceedings of the Institution of Mechanical Engineers, Part I: Journal of Systems and Control Engineering***, Vol. 233, No. 7, (2019), 815-829. (https://doi.org/10.1177%2F0959651818823450).
28. Lai, J., Yin, X., Yin, X. and Jiang, L., "Fractional order harmonic disturbance observer control for three-phase LCL-type inverter", ***Control Engineering Practice***, Vol. 107, (2021), 1-13. (https://doi.org/10.1016/j.conengprac.2020.104697).
29. Shakouri, M. and Ghadamian, H., "A energy and exergy quasi-dynamic analysis of building integrated photovoltaic system using data analytics", ***Journal of Solar Energy Research***, Vol. 4, No. 4, (2019), 273-279. (https://dx.doi.org/10.22059/jser.2020.295324.1136).
30. Mousavi, Y., Bevan, G., Küçükdemiral, I.B. and Fekih, A., "Maximum power extraction from wind turbines using a fault-tolerant fractional-order nonsingular terminal sliding mode controller", ***Energies***, Vol. 14, No. 18, (2021), 5887-5903. (https://doi.org/10.3390/en14185887).
31. Pazhanimurugan, R., Bensraj R. and Balamurugan. C.R., "Time response of FOPID controlled PV based cascaded landsman converter-inverter fed induction motor and electric drives applications", ***International Journal of Power Electronics and Drive Systems***, Vol. 11, No. 3, (2020), 1379-1387. (https://doi.org/10.11591/ijpeds.v11.i3.pp1379-1387).
32. Prasad, P., Bhaskara, P.L.M., and Sarvesh, B., "Fractional order PID controlled cascaded re-boost seven level inverter fed induction motor system with enhanced response", ***International Journal of Power Electronics and Drive Systems***, Vol. 9, No. 4, (2018), 1784-1791. (https://doi.org/10.11591/ijpeds.v9.i4.pp1784-1791).
33. Long, B., Lu, P.J., Chong, K.T., Rodriguez, J. and Guerrero, J.M., "Robust fuzzy-fractional-order nonsingular terminal sliding-mode control of a LCL-type grid-connected converter", ***IEEE Transactions on Industrial Electronics***, (2021). (https://doi.org/10.1109/TIE.2021.3094411).
34. Yousef, A.M., Abo-Elyousr, F.K., Elnozohy, A., Mohamed, M. and Abdelwahab, S.A.M., "Fractional order PI control in hybrid renewable power generation system to three phase grid connection", ***International Journal on Electrical Engineering and Informatics***, Vol. 12, No. 3, (2020), 470-493. (https://doi.org/10.15676/ijeei.2020.12.3.5).
35. Ahmed, E.M., Mohamed, E.A., Elmelegi, A., Aly, M. and Elbaksawi, O., "Optimum modified fractional order controller for future electric vehicles and renewable energy-based interconnected power systems", ***IEEE Access***, Vol. 9, (2021), 29993-30010. (https://doi.org/10.1109/ACCESS.2021.3058521).
36. Priyadarshani, S, Subhashini, K.R. and Satapathy, J.K., "Pathfinder algorithm optimized fractional order tilt-integral-derivative (FOTID) controller for automatic generation control of multi-source power system", ***Microsystem Technologies***, Vol. 27, No. 1, (2021), 23-35. (https://doi.org/10.1007/s00542-020-04897-4).
37. Banaei, M.R. and Hossein A.F.B., "A high efficiency nonisolated buck–boost converter based on ZETA converter", ***IEEE Transactions on Industrial Electronics***, Vol. 67, No. 3 (2019), 1991-1998. (https://doi.org/10.1109/TIE.2019.2902785).
38. Padmanaban, S., "An original transformer and switched-capacitor (T and SC)-based extension for DC-DC boost converter for high-voltage/low-current renewable energy applications: Hardware implementation of a new T and SC boost converter", ***Energies***, Vol. 11, No. 4, (2018), 783-806. (http://dx.doi.org/10.3390/en11040783).
39. Leyva-Ramos, J., Mota-Varona, R., Ortiz-Lopez, M. G., Diaz-Saldierna, L.H. and Langarica-Cordoba, D., "Control strategy of a quadratic boost converter with voltage multiplier cell for high-voltage gain", ***IEEE Journal of Emerging and Selected Topics in Power Electronics***, Vol. 5, No. 4, (2017), 1761-1770. (https://doi.org/10.1109/JESTPE.2017.2749311).
40. Zhang, Y., Liu, H., Li, J., Sumner, M. and Xia, C., "DC–DC boost converter with a wide input range and high voltage gain for fuel cell vehicles", ***IEEE Transactions on Power Electronics***, Vol. 34, No. 5, (2018), 4100-4111. (https://doi.org/10.1109/TPEL.2018.2858443).
41. Premkumar, K. and Shyam, D., "Design and development of N-level symmetrical multilevel inverter topology with reduced switches", ***Journal of Circuits, Systems and Computers***, Vol. 30, No. 11, 2150197.(https://doi.org/10.1142/S0218126621501978).

42. Davis, T.T. and Dey, A., "Enhanced floating capacitor voltage balancing schemes for single-source seven-level inverters with capacitor fed H-bridge units", ***IEEE Transactions on Industrial Electronics***, Vol. 67, No. 8, (2019), 6227-6236. (https://doi.org/10.1109/TIE.2019.2939976).

43. Motamarri, R. and Bhookya, N., "JAYA algorithm based on Lévy flight for global MPPT under partial shading in photovoltaic system", ***IEEE Journal of Emerging and Selected Topics in Power Electronics***, Vol. 9, No. 4, (2020), 4979-4991. (https://doi.org/10.1109/JESTPE.2020.3036405).

44. Monteghetti, F., Ghislain, H., and Matignon, D., "Stability of linear fractional differential equations with delays: A coupled parabolic-hyperbolic PDEs formulation", ***IFAC-PapersOnLine***, Vol. 50, No. 1, (2017), 13282-13288. (https://doi.org/10.1016/j.ifacol.2017.08.1966).